ACS APPLIED MATERIALS & INTERFACES

www.acsami.org

Research Article

Graphene-Enabled Vapor-Phase SERS Detection of Lithium-Ion Battery Electrolytes on Periodic Ag Nanoparticle Multimer Arrays

Maziar Moussavi,* Marjan Monshi, Gvidas Klyvis, Mantas Mikalkevičius, Mindaugas Juodėnas, Tomas Tamulevičius, and Sigitas Tamulevičius

Cite This: *ACS Appl. Mater. Interfaces* 2026, 18, 43345−43356

Read Online

ACCESS | Metrics & More | Article Recommendations | Supporting Information

ABSTRACT: Early detection of lithium-ion battery (LIB) electrolyte leakage in the vapor phase is important for battery safety, yet vapor-phase surface-enhanced Raman spectroscopy (SERS) remains challenging because weak gas−surface interactions limit analyte residence within plasmonic hot spots. Here, we report a hybrid graphene/plasmonic SERS platform for vapor-phase detection of LIB electrolyte components based on periodic Ag nanoparticle (AgNP) multimer arrays integrated with a monolayer graphene overlayer. The substrate is fabricated by capillary-assisted particle assembly (CAPA) followed by a unified poly(vinyl alcohol) (PVA)-assisted hot-press transfer process, enabling both the transfer of ordered AgNP arrays to glass and spatially selective graphene integration. This approach preserves nanoscale ordering while creating a four-region architecture on a single chip, allowing the individual and combined contributions of graphene and the plasmonic array to be evaluated under identical vapor-exposure conditions. Optical characterization shows a broadband plasmonic response dominated by interparticle coupling within AgNP multimers, with spectral overlap across the 532 nm excitation and Raman-scattering window. Upon exposure to vapors from a commercial $LiPF_6$ electrolyte containing ethylene carbonate (EC) and ethyl methyl carbonate (EMC), no analyte-attributable Raman features are observed from bare glass, graphene on glass, or the AgNP array alone. In contrast, the graphene-coated AgNP region yields clear vapor-phase Raman signatures assignable to both EC and EMC. These results show that detectable vapor-phase electrolyte signatures emerge only from the combined graphene–plasmonic architecture, consistent with a hybrid interfacial effect in which graphene may increase the local surface population of volatile molecules while the AgNP multimers provide localized electromagnetic enhancement. This work establishes a scalable hybrid-transfer strategy for ordered vapor-phase SERS substrates and highlights graphene-coated plasmonic arrays as promising material platforms for molecularly specific LIB leak detection.

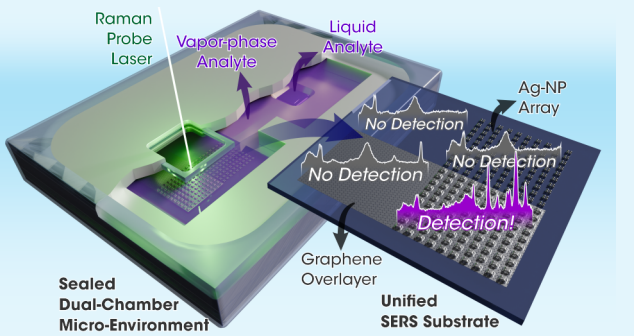

KEYWORDS: *vapor-phase SERS, lithium-ion battery electrolyte leakage, graphene, silver nanoparticle arrays, plasmonic hot spots, electrolyte vapor detection, hot-press transfer*

1. INTRODUCTION

Lithium-ion batteries (LIBs) have become indispensable across portable electronics, electric vehicles, and aerospace systems, but their high energy density is coupled to significant safety risks.[1] Catastrophic failure is often preceded by the loss of cell integrity and leakage of the liquid electrolyte, making electrolyte release one of the earliest chemically meaningful indicators of impending malfunction.[2] Commercial LIB electrolytes typically consist of $LiPF_6$ dissolved in mixtures of cyclic and linear organic carbonates such as ethylene carbonate (EC) and ethyl methyl carbonate (EMC).[3] Upon leakage, this chemistry presents a dual hazard: the solvent components are volatile and flammable, while $LiPF_6$ is highly sensitive to moisture and heat, producing toxic and corrosive decomposition products including HF, PF_5, and POF_3.[4] Consequently, even trace electrolyte leakage can act as a precursor to severe battery failure, underscoring the need for detection strategies capable of identifying vapor-phase electrolyte signatures at the earliest possible stage.[4]

Existing battery management systems primarily rely on voltage, current, and temperature monitoring, but these parameters generally respond only after substantial internal damage has already developed.[5,6] At the same time, laboratory-based analytical methods such as nuclear magnetic resonance and gas chromatography–mass spectrometry are too costly, complex, and

Received: May 1, 2026
Revised: July 14, 2026
Accepted: July 14, 2026
Published: July 23, 2026

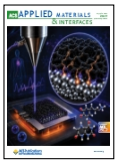

https://doi.org/10.1021/acsami.6c08906
ACS Appl. Mater. Interfaces 2026, 18, 43345−43356

bulky for practical real-time deployment in battery-powered platforms such as micromobility devices and electric vehicles.[7] To address this gap, a variety of nanostructured gas-sensing platforms have been explored for detecting electrolyte-derived vapors, including ionically conductive metal–organic frameworks and metal-oxide-based sensors.[8−11] While these systems show promise for early leakage detection, they do not inherently provide the molecular specificity needed to distinguish individual electrolyte components and their evolving chemical environment with high confidence.

Surface-enhanced Raman spectroscopy (SERS) is an attractive alternative because it combines high sensitivity with intrinsic molecular specificity.[12] In plasmonic nanostructures, SERS enhancement is primarily governed by localized surface plasmon resonance (LSPR), which amplifies Raman scattering through strongly enhanced electromagnetic fields, and can be further strengthened by nanoscale hot spots formed in narrow interparticle gaps.[13] Highly uniform nanogap structures can generate reproducible enhancement, but their effective sensing area is often limited. One route to overcoming this trade-off is to organize plasmonic nanoparticles into periodic multimers, where interparticle coupling can be combined with lattice-assisted resonances to produce large-area substrates with controlled hot-spot distributions.[13] A related chemical enhancement mechanism, arising from interfacial charge-transfer interactions, can further contribute to signal generation.[14] Importantly, SERS has already proven capable of probing electrolyte chemistry at solid–liquid interfaces, including $LiPF_6$-based carbonate systems.[15]

Despite this promise, extending SERS from liquid interfaces to vapor-phase LIB electrolyte detection remains fundamentally challenging. Gas molecules interact only weakly with bare metallic surfaces, leading to low surface coverage and short residence times within the nanometer-scale near-field volume where SERS enhancement is operative.[15] This challenge is particularly severe for highly volatile carbonate species such as EMC, which are less likely to remain localized within plasmonic hot spots long enough to produce a measurable Raman signal. In other words, a successful vapor-phase SERS platform must do more than generate strong electromagnetic enhancement: it must also increase local analyte capture at the plasmonic interface while preserving the chemical integrity of both the analyte and the active substrate.

Graphene is particularly well suited to address this bottleneck. Owing to its high surface-to-volume ratio, delocalized π-electron system, and favorable van der Waals interactions with volatile organic molecules, graphene can promote molecule–surface interactions.[16−19] When integrated with a plasmonic SERS substrate, it can serve multiple roles simultaneously: concentrating analytes near the electromagnetic hot spots, prolonging residency by analyte retention, contributing to chemical enhancement, suppressing background fluorescence, and passivating the underlying metal against environmental degradation.[16,17,20,21] Because graphene is atomically thin, these functions can be introduced without sacrificing the near-field coupling required for strong SERS enhancement. This makes graphene–plasmonic hybrids especially attractive for vapor-phase sensing at reactive solid–gas interfaces.

To the best of our knowledge, vapor-phase SERS detection of LIB electrolyte vapors such as EC, EMC, DMC, DEC, PC, or $LiPF_6$-containing carbonate electrolyte vapors has not yet been systematically reported. Previous SERS studies of battery electrolytes have primarily focused on liquid-phase or solid–liquid interfacial environments, including electrolyte solvation, SEI formation, and electrode/electrolyte reactions.[22−24] This gap highlights the need for SERS architectures that can localize volatile electrolyte molecules within plasmonic sensing regions under gas-phase exposure conditions.

Here, we report a hybrid graphene–plasmonic SERS platform designed for vapor-phase detection of components from a practically relevant LIB electrolyte formulation, namely, 1 M $LiPF_6$ in EC/EMC (30:70 w/w). The substrate combines a periodic array of Ag nanoparticle (AgNP) multimers fabricated by capillary-assisted particle assembly (CAPA) with a monolayer graphene overlayer, integrated using a unified poly(vinyl alcohol) (PVA)-assisted hot-press transfer protocol applicable to both the plasmonic array and graphene. To directly disentangle the respective roles of plasmonic enhancement and graphene-enabled interfacial effects, Raman signals were collected under identical conditions from bare glass, graphene on glass, the AgNP array on glass, and graphene-coated AgNPs integrated on a single chip. This layout enables direct side-by-side comparison of the individual and combined contributions of graphene and the plasmonic array under the same vapor-exposure and measurement conditions. Using this platform, we examine whether graphene functions only as a protective overlayer or as an active interfacial component that enables detectable vapor-phase SERS signatures of LIB electrolyte components.

2. EXPERIMENTAL SECTION

2.1. Fabrication of the Hybrid SERS Substrate

Periodic Ag nanoparticle (AgNP) multimer arrays were fabricated by combining capillary-assisted particle assembly (CAPA) with a PVA-assisted hot-press transfer process. The fabrication workflow of the hybrid four-region substrate is summarized schematically in Figure 1. Spherical AgNPs (60 ± 4 nm) were synthesized by a seeded-growth method described previously,[13,25] concentrated by centrifugation, and transferred into an ethanol/dimethylformamide mixture optimized for CAPA deposition.[13] Ordered PDMS templates containing a square lattice of nanowells (400 nm pitch, 200 nm diameter, 100 nm depth) were replicated from a silicon master, and the nanoparticle suspension was assembled into the wells by controlled meniscus translation at 2 μm s^{-1}. To favor multiparticle trapping, the assembly was performed under evaporation-driven conditions with the sample holder maintained 30 °C above the dew point, and the deposition cycle was repeated three times.[26] Under these conditions, most lattice sites were populated by compact multimers rather than isolated particles.

The assembled AgNP arrays were transferred from PDMS to glass using a PVA-assisted hot-press protocol. Briefly, a multilayer PVA support was formed on the template, laminated to a macroscopic carrier film, and hot-pressed at approximately 140 °C and 50 kPa for 120 s to obtain a freestanding transfer layer containing the ordered nanoparticle array. This layer was then laminated onto an ozone-cleaned glass under the same hot-press conditions followed by the dissolution of the PVA support in water. Ozone treatment was used to improve wetting and adhesion at the glass interface,[27] while the applied pressure promoted conformal contact during transfer.[28]

Graphene integration was then carried out using an analogous PVA-assisted transfer workflow, enabling spatially selective formation of graphene-coated and graphene-free regions on the same substrate (Figure 1e). The resulting four-region architecture was defined by the presence (1) or absence (0) of graphene (G) and the AgNP array (P): G_0P_0 (bare glass), G_1P_0 (graphene on glass), G_0P_1 (AgNP array on glass), and G_1P_1 (graphene-coated AgNP array). This integrated transfer strategy was designed to preserve nanoscale ordering while

https://doi.org/10.1021/acsami.6c08906
ACS Appl. Mater. Interfaces 2026, 18, 43345−43356

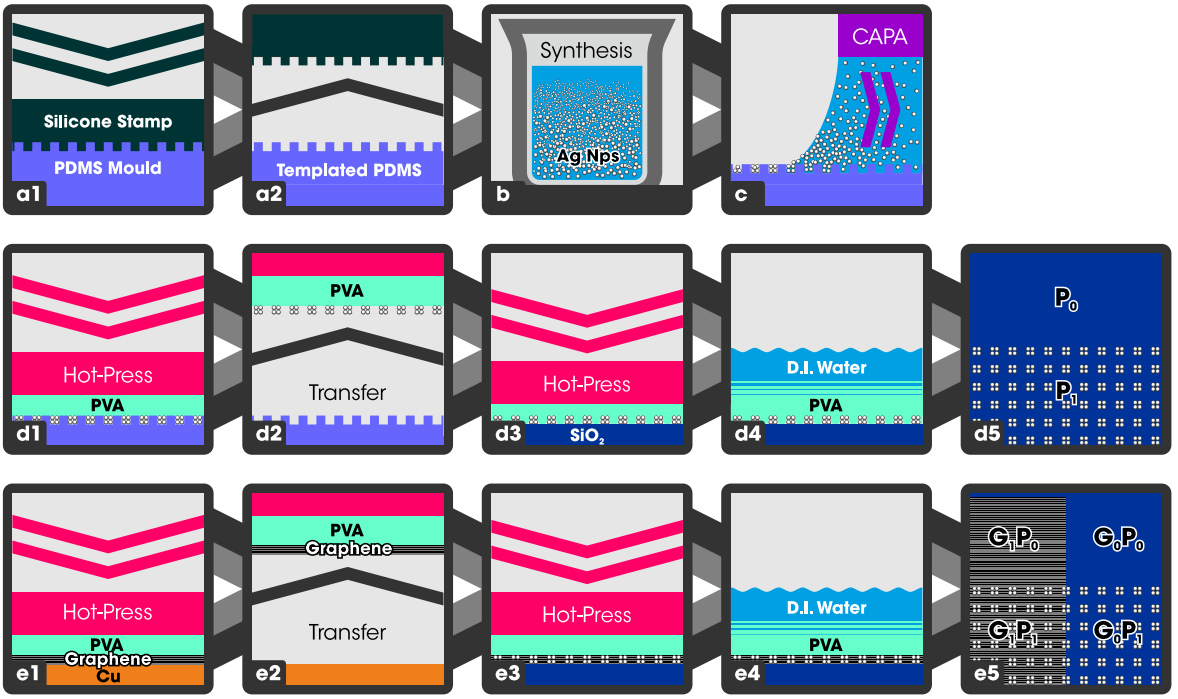

Figure 1. Schematic illustration of the fabrication of the hybrid four-region SERS substrate. (a1, a2) A PDMS template containing a square lattice of nanowells is replicated from a silicon master. (b) Monodisperse AgNPs are synthesized.(c) Nanoparticles are assembled into the template by CAPA to form an ordered multimer array.(d1–d5) The assembled AgNP array is transferred from PDMS to glass using a PVA-assisted hot-press process, defining plasmonic (P_1)and nonplasmonic (P_0) regions.(e1–e5) A monolayer graphene film is subsequently transferred onto selected areas using the same general process, producing the four-region substrate used in this study: G_1P_1, G_1P_0, G_0P_1, and G_0P_0.

enabling direct side-by-side comparison of graphene and plasmonic effects on a single substrate. Full processing details are provided in the Supporting Information.

2.2. Vapor Exposure and Raman Measurements

Vapor-phase SERS measurements were performed in a sealed dual-compartment chamber designed to expose the substrate only to electrolyte vapor while maintaining optical access through a sapphire window. The vapor-phase exposure and Raman measurement configuration are illustrated schematically in Figure 2. The chamber contained a reservoir for the liquid electrolyte source and a separate detection compartment holding the four-region SERS substrate. For each experiment, 50 μL of a commercial 1 M $LiPF_6$ electrolyte in EC/EMC (30:70 w/w) was introduced into the reservoir inside an Ar-filled glove box, after which the chamber was sealed and allowed to equilibrate for 10 min prior to Raman measurements.

Raman spectra were collected at ambient temperature (~25 °C) using a Renishaw inVia confocal Raman microscope equipped with 532 nm excitation and a 50× long-working-distance objective. The laser power at the sample was kept at ~0.5 mW, and spectra were acquired in backscattering geometry with an integration time of 100 s. For each experiment, spectra were recorded from three randomly selected locations within each of the four substrate regions. The spectra from each region were averaged, and the spatial variability of the response is shown using standard-deviation bands in the vapor-phase Raman comparison. The four-region layout ensured that all control and hybrid regions were exposed simultaneously to the same vapor atmosphere and measured under identical optical conditions.

A conventional Raman spectrum of the bulk liquid electrolyte on glass and a pre-exposure spectrum of the hybrid substrate were also recorded as reference data sets for peak assignment and background identification. Raw spectra were baseline-corrected in OriginPro and averaged within each region for comparison.

2.3. Optical Simulations

The optical response of the substrate was modeled using the finite element method in the Wave Optics module of COMSOL Multiphysics. The model consisted of a 400 × 400 nm square unit cell containing seven hexagonally packed Ag nanospheres with 60 nm diameter on a semi-infinite SiO_2 substrate with an air superstrate, representing the gaseous sensing environment. Lateral Floquet periodic boundary conditions and top/bottom perfectly matched layers were used to emulate an infinite array and suppress artificial reflections. The structure was illuminated by a normally incident plane wave, and wavelength-dependent optical constants for air, Ag, and SiO_2 were taken from literature sources.[29–31] Graphene was represented as an atomically thin conductive sheet using an effective surface-conductivity approach for thin conductive layers rather than as a finite-thickness bulk layer.[32] Absorptance and extinction spectra were calculated over the 300–700 nm range. Additional sweeps were performed to examine the effects of particle size, particle number per site, interparticle spacing, lattice periodicity, and the graphene overlayer. Details of these parameter sweeps and supporting optical measurements are summarized in the Supporting Information (Figures S1–S4).

3. RESULTS AND DISCUSSION

3.1. Structural and Optical Characterization of the Hybrid Sensing Substrate

Figure 3a shows the measured extinction spectrum of the transferred AgNP array on glass (G_0P_1). The substrate exhibits a broad optical response extending across approximately 400–650 nm, with a maximum near 500 nm, thereby overlapping both the 532 nm excitation wavelength and the corresponding Stokes-shifted Raman window used in this work. Such broad

https://doi.org/10.1021/acsami.6c08906
ACS Appl. Mater. Interfaces 2026, 18, 43345−43356

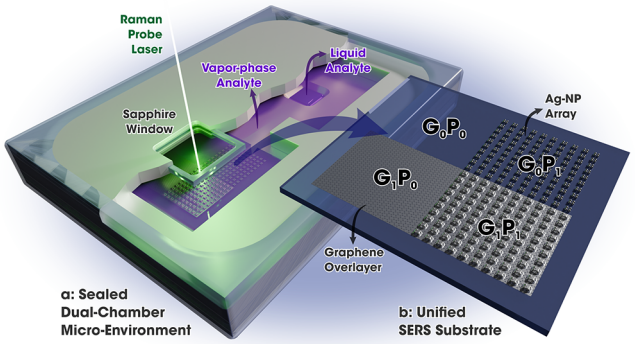

Figure 2. (a) Schematic illustration of the sealed dual-compartment microenvironment used for vapor-phase SERS measurements. The unified four-region substrate is housed in the detection compartment and exposed simultaneously to electrolyte vapors evaporating from the reservoir compartment, while Raman spectra are acquired through a sapphire window. (b) Close-up view of the unified four-region SERS substrate layout used to decouple the enhancement mechanisms: G_0P_0 (bare glass), G_1P_0 (graphene only), G_0P_1 (periodic AgNP array only), and G_1P_1 (graphene-coated AgNP array). The nanoparticles and array spacing are shown schematically and are not drawn to scale.

spectral coverage is advantageous for SERS because it can support electromagnetic enhancement across multiple vibrational bands rather than only within a narrow spectral interval.[13]

To interpret the origin of this broad response, we used finite-element simulations of representative AgNP multimer geometries together with parameter sweeps for particle size, multimer occupancy, and interparticle spacing (Figures S1–S3). These calculations show that the visible-range extinction is governed primarily by coupled plasmonic modes within the multimer sites, whose spectral position and width depend sensitively on the local cluster geometry. In addition, the periodic lattice gives rise to a weaker longer-wavelength contribution, consistent with angle-sensitive collective coupling through the surrounding media.[33]

SEM analysis of the transferred AgNP array provides experimental support for the structural variability considered in the simulations. As shown in Figure 3b and Figure S7a, the transferred array consists predominantly of compact AgNP multimers. Statistical analysis of more than 6300 array sites across ~1000 μm^2 of SEM-imaged area yielded an average occupancy of 5.8 ± 1.9 AgNPs per site (Figure S7b), confirming multiparticle site formation with expected site-to-site variation. Because top-view SEM does not unambiguously resolve the true three-dimensional gap/contact geometry of compact multimers and because the AgNPs are faceted rather than ideal spheres,[34,35] precise extraction of an interparticle gap-size distribution was not feasible. The structures are therefore described as compact AgNP multimers with nanoscale interparticle separations. Together, the observed particle size, occupancy, and local-coupling variability support interpreting the broad experimental extinction spectrum as an ensemble response rather than as a single dominant plasmonic mode.

The assignment of the longer-wavelength feature at ~618 nm to a lattice-related mode is further supported by both the lattice-period sweep in the simulations (Figure S4) and the angle-dependent measurements (Figure S5). In the simulations, this feature varies systematically with lattice periodicity, while experimentally it becomes less pronounced when the sample is tilted to 30°, consistent with the weakening of an angle-sensitive lattice contribution. These observations suggest that the

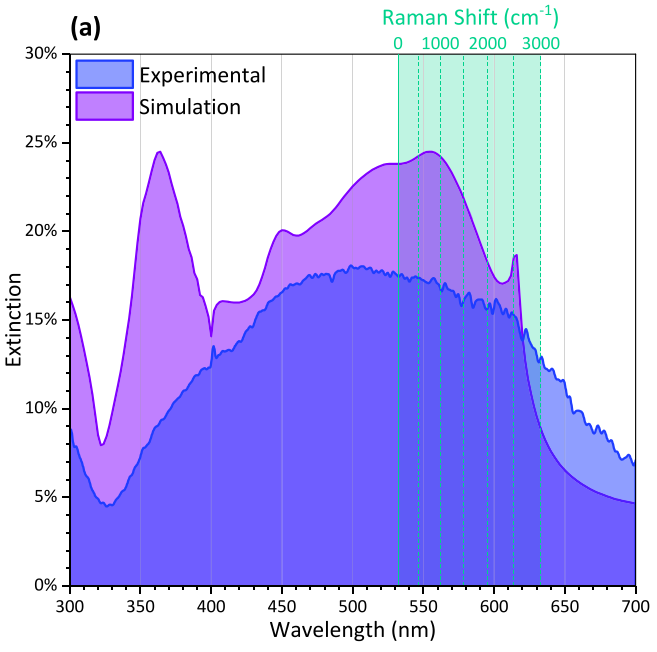

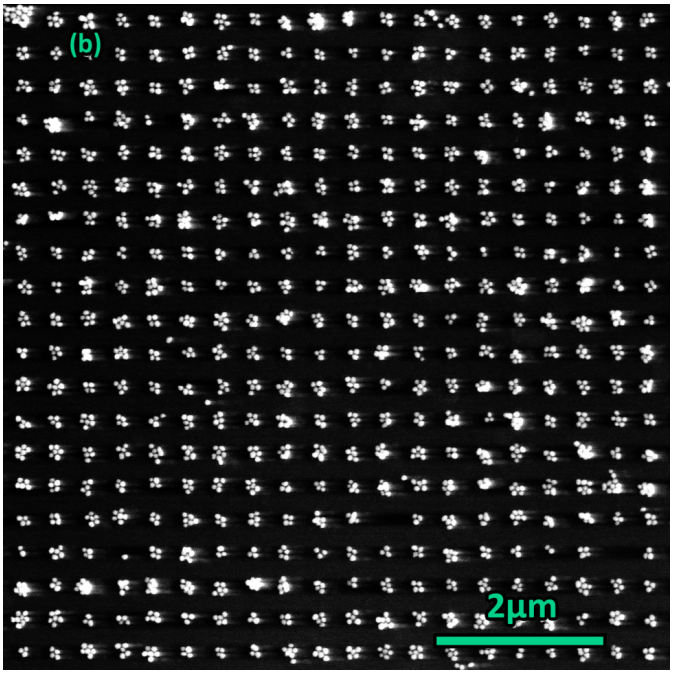

Figure 3. (a) Experimental and simulated UV–vis extinction spectra of the transferred AgNP array on glass (G_0P_1) showing a broadband optical response dominated by interparticle coupling within multimer sites, with a weaker longer-wavelength lattice-related contribution. The spectral coverage overlaps the 532 nm excitation wavelength and the Raman scattering window used in this work. (b) Representative SEM image of the transferred array after PVA removal showing a large-area square lattice of Ag nanoparticle clusters (typically two to eight particles per site) produced by CAPA and preserved during the hot-press transfer process.

https://doi.org/10.1021/acsami.6c08906
ACS Appl. Mater. Interfaces 2026, 18, 43345−43356

long-wavelength feature originates from a substrate-mediated lattice mode, likely involving diffractive coupling through the glass side of the array. Accordingly, the broad visible extinction band is dominated primarily by interparticle coupling within the multimers, while the periodic organization introduces an additional lattice-assisted contribution at larger Raman shifts.

Although localized vacancies and minor positional disorder are present, the periodic organization of the multimer sites provides a more regular structural framework than random nanoparticle monolayers, in which hot spots form stochastically, as shown in previous works.[26,36] In the present system, this ordered arrangement is therefore expected to reduce substrate-scale variability in the plasmonic architecture and to provide a more controlled basis for vapor-phase SERS measurements. The ability to form ordered plasmonic arrays and resonant Ag nanoparticle lattices is consistent with our previous work on CAPA-derived plasmonic lattices, surface lattice resonances, and graphene-overlayered Ag arrays.[13,21,37,38]

The contribution of graphene to the optical response was also examined experimentally and in the simulations. Within the investigated spectral range, the graphene overlayer produces only a minor increase in the overall extinction and does not substantially alter the plasmonic line shape of the AgNP array (Figure S6). Accordingly, graphene is not expected to act as a significant far-field electromagnetic modifier in this platform;[39,40] instead, its role is interpreted primarily as interfacial, influencing analyte capture and signal formation at the surface rather than the underlying plasmonic resonance itself.[16,21]

Raman spectroscopy was subsequently used to verify the successful transfer and quality of the graphene overlayer (Figure 4). The graphene spectrum displays the expected G band near ~1585 cm^{-1} and a sharp 2D band near ~2700 cm^{-1}, together with an intensity ratio $I_{2D}/I_G \approx 2.58$ and a relatively low defect-related ratio $I_D/I_G < 0.36$. These features are consistent with predominantly high-quality single-layer graphene with limited defect density.[16,21] For the present application, maintaining a largely intact graphene basal plane is desirable because it preserves the interfacial continuity of the coating while minimizing additional disorder-related background contributions.

The structural characterization also highlights why transferring the nanoparticle assemblies from the PDMS template to glass is essential for vapor-phase SERS measurements. In the

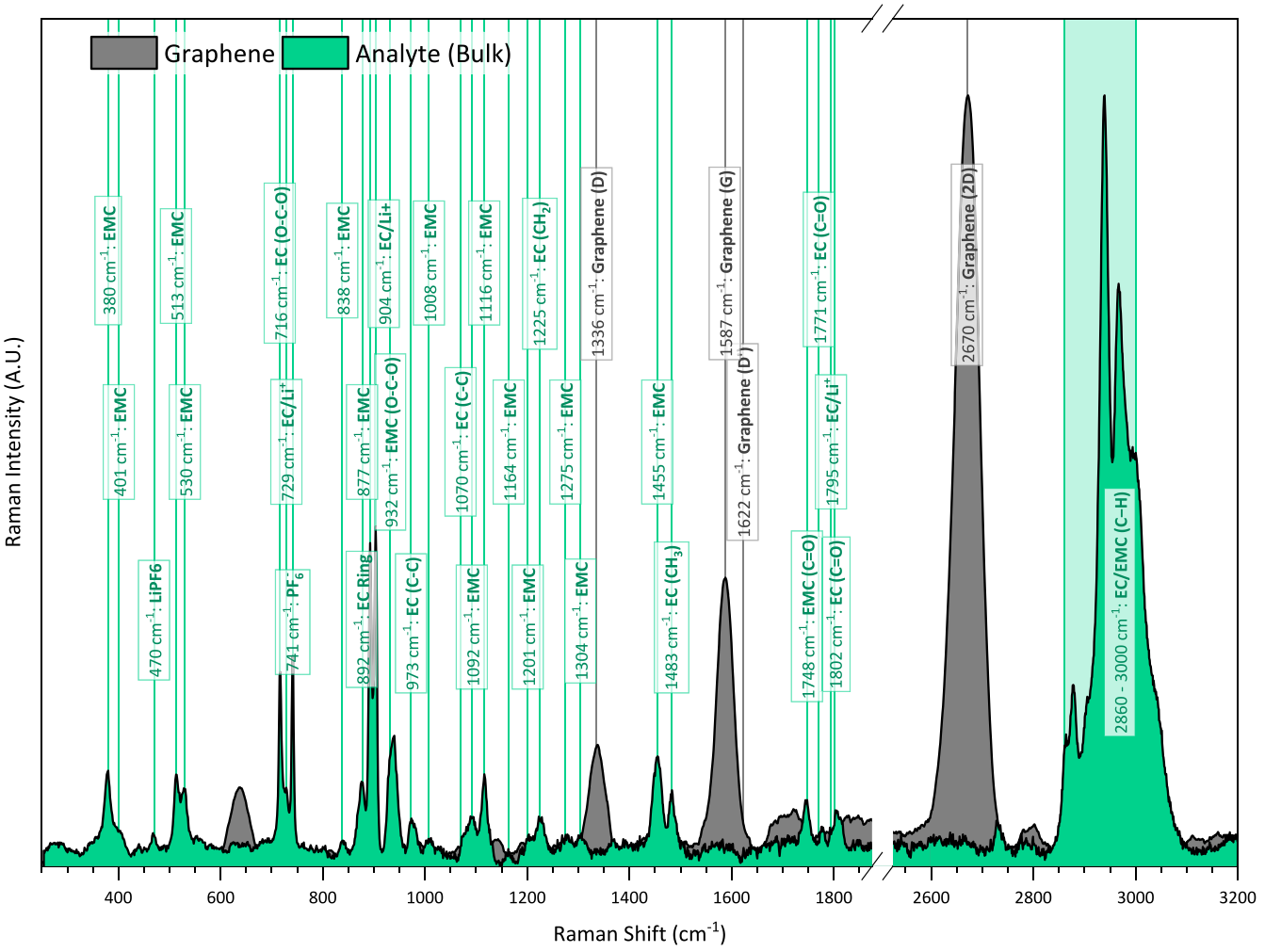

Figure 4. Reference Raman spectrum of transferred graphene (gray) and the bulk liquid LIB electrolyte (green). The baseline spectrum of 1 M $LiPF_6$ dissolved in EC/EMC (30:70 w/w) was acquired on a chemically inert glass substrate using 532 nm laser excitation. The identified characteristic peak positions are annotated according to the literature.[49]

https://doi.org/10.1021/acsami.6c08906
ACS Appl. Mater. Interfaces 2026, 18, 43345−43356

templated configuration, the multimers and their effective hot spots remain recessed inside the polymer nanowells, which would limit direct vapor access if covered by a continuous graphene overlayer, consistent with the barrier character of graphene.[41,42] After transfer, by contrast, the multimers are exposed on a planar glass surface, enabling graphene integration in direct contact with the particle topography while preserving optical access to the active interface. At the same time, replacing PDMS with glass removes the strong intrinsic Raman background of the polymer[43] and leaves only the comparatively simple glass response, thereby improving spectral interpretability for weak vapor-phase signals. The transfer step is therefore not merely a fabrication convenience but a necessary part of the substrate design for hybrid vapor-phase SERS measurements.

3.2. Raman Signature of the Liquid Electrolyte

Figure 4 presents the Raman spectrum of the bulk liquid LIB electrolyte (1 M $LiPF_6$ in EC/EMC, 30:70 w/w) together with the spectrum of the transferred graphene layer. Assignments were made based on prior Raman studies of $LiPF_6$ in carbonate electrolytes.[15,44−47] The liquid electrolyte spectrum serves as the principal vibrational reference for assigning the weaker and more localized features observed in the subsequent vapor-phase SERS measurements, while the graphene spectrum is included to distinguish intrinsic graphene bands from analyte-derived signals in the hybrid substrate.[15,48]

The bulk electrolyte spectrum contains the characteristic Raman signatures of ethylene carbonate (EC), ethyl methyl carbonate (EMC), and the $LiPF_6$ salt. Among the most diagnostically useful features are the EC ring-deformation and ring-breathing bands near ∼716 and ∼892 cm^{-1}, respectively, together with the PF_6^- symmetric stretching mode near ∼740 cm^{-1}. EMC contributes distinct bands in the ∼1000–1455 cm^{-1} range, including peaks near ∼1000, ∼1180, ∼1275, and ∼1455 cm^{-1}, which provide useful markers for identifying the linear carbonate component in the vapor-phase spectra.[15,48] The key peak assignments used in this work are summarized in Table 1.

Table 1. Key Raman Peak Assignments for Liquid Electrolyte Components (EC/EMC/$LiPF_6$)[a47]

observed Raman shift (cm^{-1})	assignment (vibrational mode, molecule/ion)
∼716	EC ring deformation
∼740	PF_6^- symmetric stretch
∼892	EC ring breathing†
∼904	EC ring breathing (Li^+ coordinated)
∼1008	EMC CH_3 rocking/O–C–O stretch†
∼1164	EMC †
∼1180	EMC C–O stretch/CH_3 rocking
∼1201	EMC
∼1275	EMC CH_2 wagging†
∼1381	EMC CH_3 symmetric deformation
∼1455	EMC CH_3/CH_2 asymmetric deformation†
∼1483	EC CH_2†
∼1775	EMC carbonyl (C═O) stretch
∼1805	EC carbonyl (C═O) stretch
∼2800–3000	EC/EMC C–H stretching modes

[a]Bands marked with † denote liquid-reference features with corresponding detectable bands in the vapor-phase G_1P_1 spectrum discussed in Section 3.3.

These reference bands are used in the following section as assignment anchors rather than as a strict one-to-one template for the interfacial SERS response. The exact Raman positions and relative intensities of electrolyte features are known to depend on local coordination and solvation environment, particularly for carbonate species interacting with Li^+ ions.[48] For example, the EC ring-breathing mode can shift from ∼892 to ∼904 cm^{-1} upon Li^+ coordination, indicating that the bulk liquid spectrum itself represents a superposition of free and coordinated species. Accordingly, small spectral shifts in the vapor-phase SERS data should be interpreted in the context of interfacial interactions and local molecular environment rather than as entirely new vibrational modes.

The bulk liquid Raman spectrum therefore provides the spectral framework required to identify the principal EC- and EMC-related features observed in the vapor-phase measurements and to distinguish them from the intrinsic graphene response of the hybrid substrate.

3.3. Vapor-Phase Raman Response of the Unified Four-Region Substrate

The central experiment of this study was the simultaneous exposure of the unified four-region substrate to LIB electrolyte vapors inside the sealed chamber, enabling direct comparison of all surface configurations under identical vapor-generation and optical measurement conditions. Figure 5 compares the baseline-corrected Raman spectra collected from the four regions—G_0P_0 (bare glass), G_1P_0 (graphene on glass), G_0P_1 (AgNP array on glass), and G_1P_1 (graphene-coated AgNP array)—after vapor exposure. For reference, the spectrum of the bulk liquid electrolyte and that of the unexposed hybrid region are also included to distinguish analyte-derived contributions from the intrinsic substrate background. This same-chip design is important because it isolates the respective roles of graphene and the plasmonic array, avoiding uncertainty arising from separate samples or different exposure histories.

As shown in Figure 5, the spatial variability of the vapor-phase Raman response was evaluated by collecting spectra from multiple randomly selected positions within each region of the same four-region chip. The averaged spectra are shown with standard-deviation bands, representing within-region variability under identical vapor-exposure and optical-measurement conditions. The electrolyte-related features are consistently resolved only in the G_1P_1 region, whereas the G_0P_0, G_1P_0, and G_0P_1 regions remain inactive within the measured variability. This supports the conclusion that the observed vapor-phase response is associated with the combined graphene–plasmonic architecture rather than with an isolated local measurement artifact.

The G_0P_0 region provides the baseline response of a nonplasmonic, nonadsorbing surface. Under the present exposure conditions, this region shows no clear Raman bands attributable to the electrolyte vapors and only weak background structure. A similarly weak response is observed from the G_0P_1 region. Although this region contains the ordered AgNP array and therefore the electromagnetic conditions required for SERS, no distinct electrolyte-related fingerprint could be resolved. Taken together, these two control regions show that neither bare glass nor the plasmonic substrate alone is sufficient for measurable vapor-phase detection in this system.

The G_1P_0 region exhibits the expected graphene Raman response, dominated by the G band near ∼1585 cm^{-1}, but does not yield a resolved vapor-phase electrolyte fingerprint beyond

https://doi.org/10.1021/acsami.6c08906
ACS Appl. Mater. Interfaces 2026, 18, 43345−43356

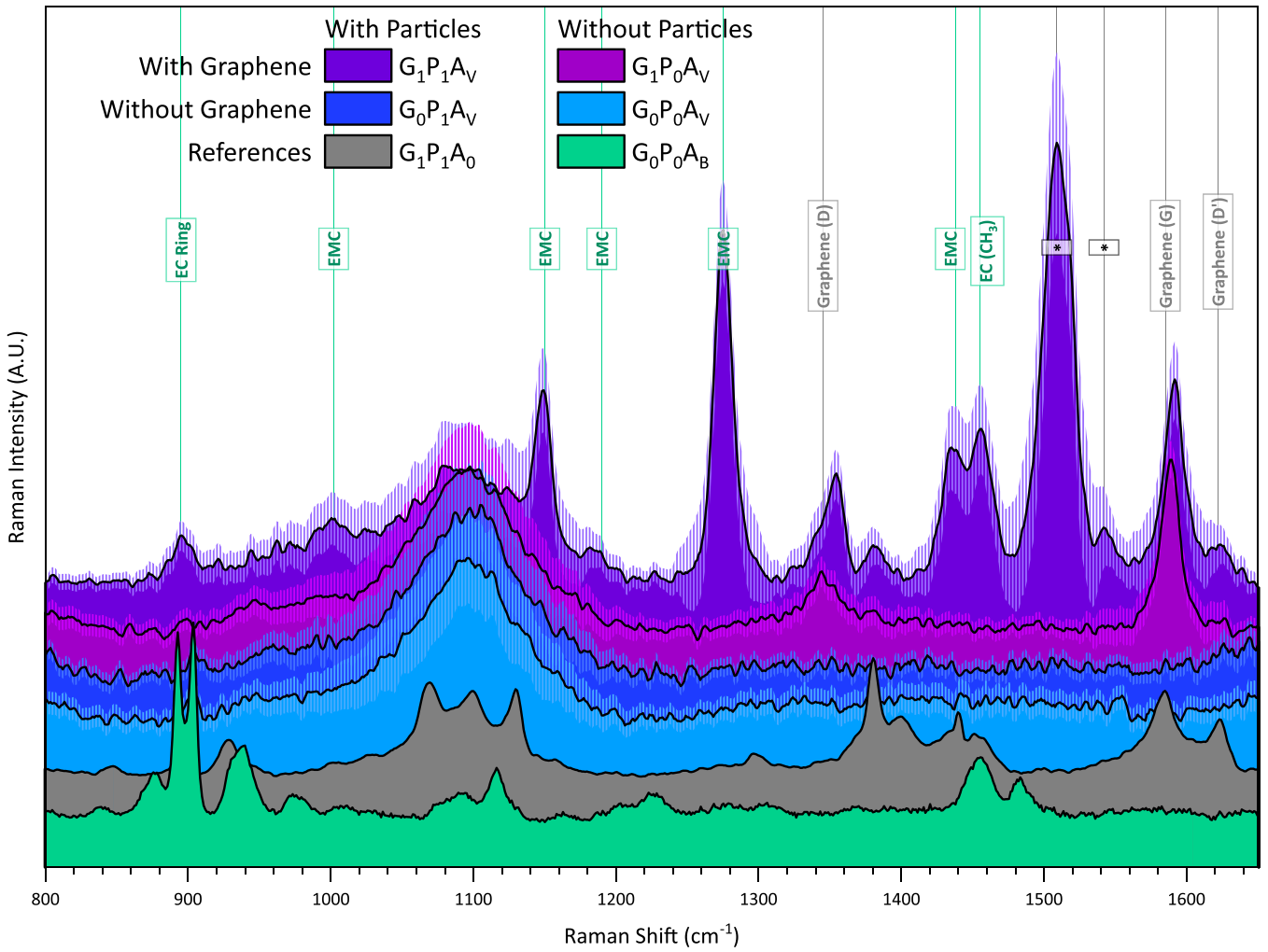

Figure 5. Baseline-corrected Raman spectra acquired after vapor exposure (A_V) from the four regions of the unified substrate: G_0P_0 (bare glass), G_1P_0 (graphene on glass), G_0P_1 (AgNP array on glass), and G_1P_1 (graphene-coated AgNP array). Solid lines represent averaged spectra collected from multiple randomly selected positions within each region, and hatched bands indicate the corresponding standard deviation. The bulk liquid electrolyte reference (A_B) and the unexposed hybrid-region spectrum (A_0) are included for comparison. Detectable vapor-phase electrolyte signatures are observed only in the graphene-coated AgNP region, highlighting the requirement for the combined graphene–plasmonic interface. Bands marked with an asterisk (*) are not assigned to the principal Raman features of the bulk analyte or substrate and are therefore treated here as unidentified vapor-exposure-related bands.

the graphene background. This indicates that graphene alone does not provide enough enhancement for practical detection under these conditions even if it may improve the adsorption of volatile species at the surface. In other words, adsorption without localized plasmonic amplification is insufficient, just as plasmonic amplification without effective analyte retention is also insufficient.

In contrast, the G_1P_1 region yields the only clearly interpretable vapor-phase Raman response, with electrolyte-related features observed consistently at multiple sampled locations within this region. Several bands appear at spectral positions consistent with the liquid electrolyte reference, with the clearest correspondence found for carbonate-solvent bands in the ~900–1500 cm^{-1} range, particularly features near ~892, ~1164, ~1275, ~1455, and ~1483 cm^{-1}. These bands are absent or not meaningfully resolved in the other three regions, indicating that a detectable vapor-phase response emerges only when graphene and the AgNP multimer array are combined. Importantly, the vapor-phase spectrum is not a simple replica of the bulk liquid spectrum. Instead, it reflects a surface-selected interfacial signature where only a subset of vibrations becomes sufficiently localized and enhanced to be detected.

Because all four regions were integrated on the same substrate and exposed simultaneously inside the sealed chamber, the comparison is not affected by differences in vapor composition, exposure time, chamber history, or optical measurement conditions. The resulting response is therefore best described as configuration-dependent vapor-phase SERS functionality: only the graphene-coated AgNP region produces molecular Raman signatures from the tested $LiPF_6$/EC/EMC vapor environment, whereas the bare glass, graphene-only, and AgNP-only regions remain inactive under the same conditions. This same-chip comparison establishes the functional requirement for combining graphene with the plasmonic AgNP multimer array in the present saturated-vapor experiment.

A notable feature of the G1P1 spectrum is the strong band at ~1509 cm^{-1}, accompanied by a weaker band near ~1542 cm^{-1}; both are unique to the graphene-coated AgNP region and absent from the bulk liquid reference and substrate background.

https://doi.org/10.1021/acsami.6c08906
ACS Appl. Mater. Interfaces 2026, 18, 43345−43356

These features are not assigned to intrinsic graphene modes or Ag, and they are not dominant bands of pristine EC/EMC/$LiPF_6$. As summarized in Section S4 and Table S2, literature Raman/SERS data place bulk EC bands mainly below ~1500 cm^{-1},[50] carbonate-derived $ROCO_2Li$-like surface species near 1493–1519 cm^{-1},[22,23] and graphene-induced molecular frequency shifts on the order of tens of cm^{-1}.[51] Therefore, the ~1509 cm^{-1} band is tentatively interpreted as a surface-confined carbonate-derived species or lithium alkyl carbonate-like intermediate whose frequency may be modified by the graphene/Ag surface environment. The ~1542 cm^{-1} band remains unresolved and is treated as a vapor-exposure-related feature associated with a surface-confined or graphene/Ag-modified molecular configuration rather than as a direct replica of bulk EC/EMC Raman modes.

Overall, the four-region comparison establishes a clear hierarchy of sensing performance. Bare glass shows no useful vapor response, graphene on glass shows adsorption without sufficient enhancement, and the AgNP array on glass provides a plasmonic structure without detectable analyte capture. Only the graphene-coated AgNP array produces a resolved vapor-phase Raman signature of the LIB electrolyte. The most consistent interpretation is therefore that vapor detection in this system arises from a hybrid interfacial effect: the AgNP multimers generate the localized electromagnetic hot spots required for signal amplification, while graphene may increase the local surface population or residence probability of volatile electrolyte molecules near the active sensing region. In this sense, graphene acts not merely as a passive overlayer but as an essential functional component of the vapor-phase sensing interface.

3.4. Discussion of Enhancement Mechanisms and Synergy

The same-chip comparison therefore points to a hybrid interfacial sensing mechanism rather than to plasmonic enhancement or graphene adsorption alone. A central limitation of vapor-phase SERS is the extreme spatial confinement of electromagnetic enhancement. In plasmonic nanoparticle systems, the enhanced field is concentrated in the immediate vicinity of the metal surface and is strongest in nanometer-scale interparticle gaps, decaying rapidly away from these hot spots.[52,53] Under vapor exposure, the key challenge is therefore not simply whether analyte molecules are present in the chamber but whether they can reach and remain within this highly confined sensing volume long enough to contribute a measurable Raman signal. The absence of resolved electrolyte bands in G_0P_1 suggests that, under the present conditions, the AgNP multimer array alone does not provide sufficient local analyte occupancy despite supplying the required electromagnetic hot spots.

The role of graphene in G_1P_1 is therefore interpreted primarily as interfacial rather than electromagnetic. Both the optical measurements and the simulations indicate that adding graphene produces only a minor change in the far-field extinction response of the AgNP array, supporting the conclusion that graphene does not substantially reshape the plasmonic resonance itself.[36,39] Its contribution is more plausibly associated with increasing the local residence probability or surface population of volatile carbonate molecules near the plasmonically active AgNP hot spots,[16–19] while also helping suppress background and parasitic surface chemistry, consistent with prior graphene–SERS studies.[16,21,51,54–58]

This interpretation is consistent with prior studies showing that graphene can interact with molecular adsorbates through noncovalent mechanisms, including dispersion/van der Waals and π–π interactions.[59–61] Benzene adsorption on supported graphene has been characterized by thermal desorption spectroscopy,[59] while theoretical studies report benzene–graphene binding energies on the order of ~40 kJ mol^{-1} and show that aromatic molecule–graphene adhesion is dominated primarily by dispersion interactions.[60,61] Graphene-enhanced Raman studies have further shown that molecule–graphene contact can produce Raman enhancement, frequency shifts, molecular selectivity, and charge-transfer-related effects.[51,57,58] In addition, graphene-based vapor sensors have been reported to respond to volatile organic compounds through adsorption-related mechanisms at graphene or graphene-composite surfaces.[62] Our previous work on graphene-overlayered resonant Ag nanoparticle arrays showed long-term retention of an aromatic analyte Raman signature, providing relevant precedent for graphene-assisted analyte localization and signal stabilization in graphene/plasmonic SERS architectures.[21]

The vapor-phase G_1P_1 spectrum also differs from the bulk liquid reference, indicating that the detected signal is surface-selected rather than a simple diluted replica of the liquid electrolyte. The G_1P_1-only bands near ~1509 and ~1542 cm^{-1}, discussed in Section S4 and Table S2, further support this surface-selected character and are most cautiously treated as vapor-exposure-related features associated with surface-confined or graphene/Ag-modified molecular configurations. This cautious interpretation is also consistent with the known chemical reactivity of $LiPF_6$-based carbonate electrolytes under environmental exposure.[63]

Overall, the results support a mechanistic picture in which the AgNP multimers provide localized electromagnetic enhancement, while graphene may increase the local surface population or residence probability of volatile electrolyte molecules near the active sensing region, enabling a chemically interpretable vapor-phase Raman signal to emerge.[16,21]

3.5. Contextualizing Detection Sensitivity and Nanoscale Confinement

To place the observed SERS signals in the context of practical battery monitoring, it is essential to consider the relationship between the equilibrium vapor pressures of the electrolyte components and the active sensing volume of the substrate. At 25 °C, the cyclic carbonate EC exhibits a very low vapor pressure of approximately 5.2 Pa, whereas the linear carbonate EMC is highly volatile with a vapor pressure of roughly 4300 Pa. Assuming ideal gas behavior and full equilibrium saturation within the sealed experimental chamber, these pressures translate to upper-bound bulk vapor concentrations of roughly 51 ppm for EC and 42,400 ppm (4.24% by volume) for EMC.[64]

Although the vapor pressures of the electrolyte components provide a useful chamber-scale estimate of analyte availability, the present results should not be interpreted as a complete quantitative sensor calibration or as a calibrated gas-phase detection limit. At 25 °C, EC and EMC differ strongly in volatility, implying very different equilibrium vapor concentrations above the electrolyte reservoir; however, the Raman signal in this system does not originate from the chamber-average vapor composition but from molecules residing within the nanometer-scale near-field volume of the plasmonic hot spots. In this sense, the decisive challenge of vapor-phase SERS is not simply analyte presence in the gas phase but efficient localization of molecules at the active graphene–plasmonic interface. Accordingly, the present measurements should be viewed as a proof-of-concept demonstration that

https://doi.org/10.1021/acsami.6c08906
ACS Appl. Mater. Interfaces 2026, 18, 43345–43356

the hybrid substrate architecture can convert vapor exposure into a chemically interpretable Raman response.

To place the present proof-of-concept in the context of reported LIB electrolyte vapor sensors, it is useful to distinguish between calibrated gas-sensing performance and molecularly specific spectroscopic identification. Several non-SERS approaches have demonstrated impressive analytical performance for LIB electrolyte leakage detection. Commercial metal-oxide volatile organic compound (VOC) sensors can detect broad classes of solvent vapors in the ppm range and have been proposed for battery safety monitoring.[65] Functionalized double-walled carbon nanotube sensors have been reported for DMC vapor and electrolyte leakage detection, with clear response to leakage levels as low as 0.1 μL DMC.[66] Ionically conductive MOF thin-film sensors have achieved rapid detection of 50 ppb DMC and 20 nL electrolyte leakage within seconds.[9] Metal-oxide semiconductor sensors, including $TiO_2/CuO/Cu_2O$ heterostructures, SnO_2 nanoboxes, porous SnO_2 nanonets, and $Ag@Ag_2O$-functionalized SnO_2 nanoflowers, have also shown ppb–ppm detection of carbonate electrolyte vapors, often with rapid response/recovery but typically using elevated operating temperatures.[10,67,68] More recently, COF-QA-4 chemiresistive sensors were reported to detect EC vapor at 1.15 ppmv, where ppmv denotes parts per million by volume,[69] while ZIF-8-coated micro–nano optical-fiber sensors achieved ppm-level DMC detection and online leakage monitoring.[70] Compared with calibrated chemiresistive, electrical, and refractive-index-based sensors, the present graphene–plasmonic SERS platform is not yet optimized for LoD, response/recovery kinetics, or cycling stability. Its main distinction is instead molecular specificity: the Raman spectrum provides vibrational fingerprints of electrolyte-related species, allowing spectral identification rather than only a scalar electrical or optical response. The same-chip four-region experiment further demonstrates that detectable vapor-phase electrolyte signatures emerge only from the combined graphene-coated AgNP region, establishing the functional requirement for the hybrid graphene–plasmonic architecture under saturated vapor exposure.

The present saturated-vapor experiment establishes the functional requirement for the combined graphene–plasmonic architecture and demonstrates molecularly specific Raman detection from the tested $LiPF_6$/EC/EMC vapor environment. Translation toward a calibrated vapor sensor will require controlled vapor-delivery experiments to quantify analytical figures of merit such as LoD, concentration dependence, response/recovery behavior, cycling stability, interferent tolerance, and adsorption/retention behavior. These follow-up measurements will complement the present same-chip mechanistic comparison by connecting the observed molecular SERS response to practical sensor-performance metrics.

4. CONCLUSIONS

We developed a hybrid graphene–plasmonic substrate for vapor-phase SERS detection of lithium-ion battery electrolyte components by combining capillary-assisted particle assembly with a PVA-assisted hot-press transfer process. This approach enabled ordered AgNP multimer arrays to be transferred from the PDMS template to glass and allowed spatially selective graphene integration on the same substrate. The resulting four-region architecture provided a direct same-chip comparison of bare glass, graphene on glass, AgNP arrays, and graphene-coated AgNP arrays under identical vapor-exposure conditions.

Optical characterization and simulations show that the plasmonic response is governed primarily by interparticle coupling within AgNP multimers, while the graphene overlayer produces only a minor change in the far-field extinction spectrum. Under exposure to vapors from a $LiPF_6$/EC/EMC electrolyte, analyte-attributable Raman features were not observed from bare glass, graphene on glass, or the AgNP array alone. In contrast, clear vapor-phase Raman signatures assignable to EC and EMC, including characteristic carbonate-solvent bands in the ~900–1500 cm^{-1} region, were obtained only from the graphene-coated AgNP region.

While previous SERS studies of LIB electrolytes have primarily addressed liquid-phase or solid–liquid interfacial environments, this work helps establish vapor-phase SERS as a complementary route for molecularly specific electrolyte-leakage detection. These results support a hybrid interfacial sensing mechanism in which the ordered AgNP multimers provide localized electromagnetic enhancement, while graphene may increase the local surface population or residence probability of volatile electrolyte molecules near the active sensing region. The work identifies graphene-coated periodic AgNP multimer arrays as a promising material platform for molecularly specific vapor-phase detection of LIB electrolyte leakage and establishes PVA-assisted hot-press transfer as a useful route for constructing hybrid graphene–plasmonic sensing interfaces.

■ ASSOCIATED CONTENT

Data Availability Statement

The data underlying this study are available in the article and its Supporting Information. Additional data sets generated during the current study are available from the corresponding author upon reasonable request.

Supporting Information

The Supporting Information is available free of charge at https://pubs.acs.org/doi/10.1021/acsami.6c08906.

Section S1, detailed experimental procedures for Ag nanoparticle synthesis and solvent exchange, PDMS template fabrication, capillary-assisted particle assembly, PVA-assisted hot-press transfer, graphene transfer, four-region substrate formation, vapor-exposure chamber, and Raman measurements, including *Table S1* on key electrolyte properties; **Section S2**, extended electromagnetic simulation and optical characterization results, including *Figures S1–S6* on nanoparticle diameter, multimer occupancy, interparticle spacing, lattice periodicity, experimental angle dependence, and graphene overcoating effects; **Section S3**, SEM-based AgNP multimer occupancy analysis, including *Figure S7* showing representative SEM images, higher-magnification multimer views, and the particle-number-per-site occupancy histogram; and **Section S4**, literature context for emergent vapor-phase bands, including *Table S2* summarizing relevant Raman/SERS reports for carbonate electrolytes, carbonate-derived surface species, and graphene-enhanced Raman systems (PDF)

■ AUTHOR INFORMATION

Corresponding Author

Maziar Moussavi – *Institute of Materials Science, Kaunas University of Technology, K. Baršausko St. 59, Kaunas LT-51423, Lithuania;* orcid.org/0000-0003-4108-9454; Email: Maziar.Moussavi@ktu.lt

https://doi.org/10.1021/acsami.6c08906
ACS Appl. Mater. Interfaces 2026, 18, 43345–43356

Authors

Marjan Monshi – *Institute of Materials Science, Kaunas University of Technology, K. Baršausko St. 59, Kaunas LT-51423, Lithuania*

Gvidas Klyvis – *Institute of Materials Science, Kaunas University of Technology, K. Baršausko St. 59, Kaunas LT-51423, Lithuania*

Mantas Mikalkevičius – *Institute of Materials Science, Kaunas University of Technology, K. Baršausko St. 59, Kaunas LT-51423, Lithuania*; orcid.org/0000-0002-5305-5676

Mindaugas Juodėnas – *Institute of Materials Science, Kaunas University of Technology, K. Baršausko St. 59, Kaunas LT-51423, Lithuania*; orcid.org/0000-0002-0517-8620

Tomas Tamulevičius – *Institute of Materials Science, Kaunas University of Technology, K. Baršausko St. 59, Kaunas LT-51423, Lithuania; Department of Physics, Kaunas University of Technology, Studentų St. 50, Kaunas LT-51368, Lithuania*; orcid.org/0000-0003-3879-2253

Sigitas Tamulevičius – *Institute of Materials Science, Kaunas University of Technology, K. Baršausko St. 59, Kaunas LT-51423, Lithuania; Department of Physics, Kaunas University of Technology, Studentų St. 50, Kaunas LT-51368, Lithuania*; orcid.org/0000-0002-9965-2724

Complete contact information is available at: https://pubs.acs.org/doi/10.1021/acsami.6c08906

Author Contributions

Maziar Moussavi: Conceptualization, Methodology, Investigation, Formal analysis, Writing–original draft, Writing–review & editing, Visualization. Marjan Monshi: Methodology, Validation, Investigation. Gvidas Klyvis: Methodology, Validation, Investigation. Mantas Mikalkevičius: Methodology, Resources. Mindaugas Juodėnas: Methodology, Validation, Investigation, Resources, Writing–review & editing. Tomas Tamulevičius: Validation, Resources, Funding acquisition, Writing–review & editing. Sigitas Tamulevičius: Conceptualization, Methodology, Validation, Resources, Writing–review & editing, supervision, project administration

Notes

Microsoft 365 Copilot was used during manuscript preparation to assist in revising selected text passages for clarity, organization, and style. The tool was not used to generate data, references, or scientific conclusions. All outputs were critically reviewed, modified where necessary, and approved by the authors, who assume full responsibility for the content of the submitted manuscript.

The authors declare no competing financial interest.

■ ACKNOWLEDGMENTS

Research was conducted as part of the execution of Project "Mission-driven Implementation of Science and Innovation Programmes" (No. 02-002-P-0001), funded by the Economic Recovery and Resilience Plan "New Generation Lithuania".

■ REFERENCES

(1) Rinkel, B. L. D.; Hall, D. S.; Temprano, I.; Grey, C. P. Electrolyte Oxidation Pathways in Lithium-Ion Batteries. *J. Am. Chem. Soc.* **2020**, *142* (35), 15058–15074.

(2) Pandey, I.; Tiwari, J. D. Advance Sensor for Monitoring Electrolyte Leakage in Lithium-Ion Batteries for Electric Vehicles (**2022**). *9th IEEE Uttar Pradesh Section International Conference on Electrical, Electronics and Computer Engineering*; UPCON 2022.

(3) Zhang, S. S.; Jow, T. R.; Amine, K.; Henriksen, G. L. LiPF6–EC–EMC Electrolyte for Li-Ion Battery. *J. Power Sources* **2002**, *107* (1), 18–23.

(4) Lu, X.; Tarascon, J.-M.; Huang, J. Perspective on Commercializing Smart Sensing for Batteries. *eTransportation* **2022**, *14*, No. 100207.

(5) Pokorný, V.; Štejfa, V.; Fulem, M.; Červinka, C.; Růžička, K. Vapor Pressures and Thermophysical Properties of Ethylene Carbonate, Propylene Carbonate, γ-Valerolactone, and γ-Butyrolactone. *J. Chem. Eng. Data* **2017**, *62* (12), 4174–4186.

(6) Gervillié-Mouravieff, C.; Boussard-Plédel, C.; Huang, J.; Leau, C.; Blanquer, L. A.; Yahia, M. Ben; Doublet, M. L.; Boles, S. T.; Zhang, X. H.; Adam, J. L.; Tarascon, J. M. Unlocking Cell Chemistry Evolution with Operando Fibre Optic Infrared Spectroscopy in Commercial Na(Li)-Ion Batteries. *Nat. Energy* **2022**, *7* (12), 1157–1169.

(7) Dotoli, M.; Rocca, R.; Giuliano, M.; Nicol, G.; Parussa, F.; Baricco, M.; Ferrari, A. M.; Nervi, C.; Sgroi, M. F. A Review of Mechanical and Chemical Sensors for Automotive Li-Ion Battery Systems. *Sensors* **2022**, *22* (5), 1763.

(8) Lupan, O.; Magariu, N.; Santos-Carballal, D.; Ababii, N.; Offermann, J.; Pooker, P.; Hansen, S.; Siebert, L.; de Leeuw, N. H.; Adelung, R. Development of 2-in-1 Sensors for the Safety Assessment of Lithium-Ion Batteries via Early Detection of Vapors Produced by Electrolyte Solvents. *ACS Appl. Mater. Interfaces* **2023**, *15* (22), 27340–27356.

(9) Lu, Y.; Zhang, S.; Dai, S.; Liu, D.; Wang, X.; Tang, W.; Guo, X.; Duan, J.; Luo, W.; Yang, B.; Zou, J.; Huang, Y.; Katz, H. E.; Huang, J. Ultrasensitive Detection of Electrolyte Leakage from Lithium-Ion Batteries by Ionically Conductive Metal-Organic Frameworks. *Matter* **2020**, *3* (3), 904–919.

(10) Sun, X. Q.; Li, Y. F.; Chen, L.; Li, H. B.; Gao, R. H.; Liu, J.; Yang, T. Y.; Guo, Z. Universal Gas-Sensitive Detection of Various Lithium-Ion Battery Electrolyte Leakages via Ag@Ag2O-Functionalized SnO2 Nanoflowers with Abundant Oxygen Vacancies. *Anal. Chem.* **2025**, *97* (6), 3589–3599.

(11) Cao, P.; Qu, L.; Jia, F.; Zeng, Y.; Zhu, D.; Wang, C.; Han, S.; Fang, M.; Liu, X.; Liu, W.; Navale, S. T. Three-Dimensional Ordered Porous SnO2 Nanostructures Derived from Polystyrene Sphere Templates for Ethyl Methyl Carbonate Detection in Battery Safety Applications. *Nanomaterials* **2025**, *15* (15), 1150.

(12) Mosier-Boss, P. A. Review of SERS Substrates for Chemical Sensing. *Nanomaterials* **2017**, *7* (6), 142.

(13) Khinevich, N.; Juodėnas, M.; Tamulevičienė, A.; Tamulevičius, T.; Talaikis, M.; Niaura, G.; Tamulevičius, S. Wavelength-Tailored Enhancement of Raman Scattering on a Resonant Plasmonic Lattice. *Sens. Actuators, B* **2023**, *394*, No. 134418.

(14) Moldovan, R.; Vereshchagina, E.; Milenko, K.; Iacob, B. C.; Bodoki, A. E.; Falamas, A.; Tosa, N.; Muntean, C. M.; Farcău, C.; Bodoki, E. Review on Combining Surface-Enhanced Raman Spectroscopy and Electrochemistry for Analytical Applications. *Anal. Chim. Acta* **2022**, *1209*, No. 339250.

(15) Yang, G.; Ivanov, I. N.; Ruther, R. E.; Sacci, R. L.; Subjakova, V.; Hallinan, D. T.; Nanda, J. Electrolyte Solvation Structure at Solid–Liquid Interface Probed by Nanogap Surface-Enhanced Raman Spectroscopy. *ACS Nano* **2018**, *12* (10), 10159–10170.

(16) Lai, H.; Xu, F.; Zhang, Y.; Wang, L. Recent Progress on Graphene-Based Substrates for Surface-Enhanced Raman Scattering Applications. *J. Mater. Chem. B* **2018**, *6* (24), 4008–4028.

(17) Lebedev, A. A.; Lebedev, S. P.; Novikov, S. N.; Davydov, V. Y.; Smirnov, A. N.; Litvin, D. P.; Makarov, Y. N.; Levitskii, V. S. Supersensitive Graphene-Based Gas Sensor. *Tech. Phys.* **2016**, *61* (3), 453–457.

(18) Teli, A. M.; Mane, S. M.; Beknalkar, S. A.; Mishra, R. K.; Jeon, W.; Shin, J. C. Graphene-Based Gas Sensors: State-of-the-Art Developments for Gas Sensing Applications. *Micromachines* **2025**, *16* (8), 916.

(19) Phung, V. B. T.; Tran, T. N.; Tran, Q. H.; Luong, T. T.; Dinh, V. A. Graphene as a Sensor for Lung Cancer: Insights into Adsorption of VOCs Using VdW DFT. *ACS Omega* **2024**, *9* (2), 2302–2313.
(20) Zhang, X.; Si, S.; Zhang, X.; Wu, W.; Xiao, X.; Jiang, C. Improved Thermal Stability of Graphene-Veiled Noble Metal Nanoarrays as Recyclable SERS Substrates. *ACS Appl. Mater. Interfaces* **2017**, *9* (46), 40726–40733.
(21) Monshi, M.; Moussavi, M.; Khinevich, N.; Tamulevičius, T.; Tamulevičienė, A.; Henzie, J.; Juodėnas, M.; Tamulevičius, S. Graphene-Enhanced Resonant Arrays of Silver Nanoparticles for Sustained Detection of Raman Signature. *J. Phys. Chem. C* **2025**, *129* (33), 14983–14992.
(22) Li, H.; Mo, Y.; Pei, N.; Xu, X.; Huang, X.; Chen, L. Surface-Enhanced Raman Scattering Study on Passivating Films of Ag Electrodes in Lithium Batteries†. *J. Phys. Chem. B* **2000**, *104* (35), 8477–8480.
(23) Li, G.; Li, H.; Mo, Y.; Chen, L.; Huang, X. Further Identification to the SEI Film on Ag Electrode in Lithium Batteries by Surface Enhanced Raman Scattering (SERS). *J. Power Sources* **2002**, *104* (2), 190–194.
(24) Hy, S.; Felix; Chen, Y. H.; Liu, J. Y.; Rick, J.; Hwang, B. J. In Situ Surface Enhanced Raman Spectroscopic Studies of Solid Electrolyte Interphase Formation in Lithium Ion Battery Electrodes. *J. Power Sources* **2014**, *256*, 324–328.
(25) Bastús, N. G.; Merkoçi, F.; Piella, J.; Puntes, V. Synthesis of Highly Monodisperse Citrate-Stabilized Silver Nanoparticles of up to 200 Nm: Kinetic Control and Catalytic Properties. *Chem. Mater.* **2014**, *26* (9), 2836–2846.
(26) Virganavičius, D.; Juodėnas, M.; Tamulevičius, T.; Schift, H.; Tamulevičius, S. Investigation of Transient Dynamics of Capillary Assisted Particle Assembly Yield. *Appl. Surf. Sci.* **2017**, *406*, 136–143.
(27) Verding, P.; Mary Joy, R.; Reenaers, D.; Kumar, R. S. N.; Rouzbahani, R.; Jeunen, E.; Thomas, S.; Desta, D.; Boyen, H. G.; Pobedinskas, P.; Haenen, K.; Deferme, W. The Influence of UV–Ozone, O2 Plasma, and CF4 Plasma Treatment on the Droplet-Based Deposition of Diamond Nanoparticles. *ACS Appl. Mater. Interfaces* **2023**, *16* (1), 1719–1726.
(28) Ahn, J.; Jang, H.; Jeong, Y.; Choi, S.; Ko, J.; Hwang, S. H.; Jeong, J. H.; Jung, Y. S.; Park, I. Illuminating Recent Progress in Nanotransfer Printing: Core Principles, Emerging Applications, and Future Perspectives. *Adv. Sci.* **2023**, *11* (1), No. 2303704.
(29) Börzsönyi, A.; Heiner, Z.; Kalashnikov, M. P.; Kovács, A. P.; Osvay, K. Dispersion Measurement of Inert Gases and Gas Mixtures at 800 Nm. *Appl. Opt.* **2008**, *47* (27), 4856-4863.
(30) Ferrera, M.; Magnozzi, M.; Bisio, F.; Canepa, M. Temperature-Dependent Permittivity of Silver and Implications for Thermoplasmonics. *Phys. Rev. Mater.* **2019**, *3* (10), No. 105201.
(31) Ghosh, G. Dispersion-Equation Coefficients for the Refractive Index and Birefringence of Calcite and Quartz Crystals. *Opt. Commun.* **1999**, *163* (1–3), 95–102.
(32) Andryieuski, A.; Lavrinenko, A. V; Bolotin, K.; Sikes, K.; Jiang, Z.; Klima, M.; Fudenberg, G.; Hone, J.; Kim, P.; Stormer, H. Graphene Metamaterials Based Tunable Terahertz Absorber: Effective Surface Conductivity Approach. *Opt. Express* **2013**, *21* (7), 9144–9155.
(33) Fan, J. A.; Bao, K.; Sun, L.; Bao, J.; Manoharan, V. N.; Nordlander, P.; Capasso, F. Plasmonic Mode Engineering with Templated Self-Assembled Nanoclusters. *Nano Lett.* **2012**, *12* (10), 5318–5324.
(34) Klinavičius, T.; Khinevich, N.; Tamulevičienė, A.; Vidal, L.; Tamulevičius, S.; Tamulevičius, T. Deep Learning Methods for Colloidal Silver Nanoparticle Concentration and Size Distribution Determination from UV–Vis Extinction Spectra. *J. Phys. Chem. C* **2024**, *128* (23), 9662–9675.
(35) Khinevich, N.; Peckus, D.; Tamulevičienė, A.; Klimaitė, G.; Henzie, J.; Tamulevičius, T.; Tamulevičius, S. Size and Crystallinity Effect on the Ultrafast Optical Response of Chemically Synthesized Silver Nanoparticles. *J. Materiomics* **2024**, *10* (3), 594–600.
(36) Juodenas, M.; Tamulevičius, T.; Henzie, J.; Erts, D.; Tamulevičius, S. Surface Lattice Resonances in Self-Assembled Arrays of Monodisperse Ag Cuboctahedra. *ACS Nano* **2019**, *13* (8), 9038–9047.
(37) Andrzejewska, W.; Khinevich, N.; Obstarczyk, P.; Murawka, S.; Tamulevičius, T.; Olesiak-Bańska, J.; Tamulevičius, S.; Lewandowski, M. Towards Ultrasensitive Biosensors Based on Virus-like Particles and Plasmonic Surface Lattice Resonance. *Biosens. Bioelectron.* **2025**, *274*, No. 117143.
(38) Juodėnas, M.; Khinevich, N.; Klyvis, G.; Henzie, J.; Tamulevičius, T.; Tamulevičius, S. Lasing in an Assembled Array of Silver Nanocubes. *Nanoscale Horiz.* **2024**, *10* (1), 142–149.
(39) Zhu, S. E.; Yuan, S.; Janssen, G. C. A. M. Optical Transmittance of Multilayer Graphene. *Europhys. Lett.* **2014**, *108* (1), No. 17007.
(40) Nair, R. R.; Blake, P.; Grigorenko, A. N.; Novoselov, K. S.; Booth, T. J.; Stauber, T.; Peres, N. M. R.; Geim, A. K. Fine Structure Constant Defines Visual Transparency of Graphene. *Science* **2008**, *320* (5881), 1308.
(41) Berry, V. Impermeability of Graphene and Its Applications. *Carbon* **2013**, *62*, 1–10.
(42) Sun, P. Z.; Yang, Q.; Kuang, W. J.; Stebunov, Y. V.; Xiong, W. Q.; Yu, J.; Nair, R. R.; Katsnelson, M. I.; Yuan, S. J.; Grigorieva, I. V.; Lozada-Hidalgo, M.; Wang, F. C.; Geim, A. K. Limits on Gas Impermeability of Graphene. *Nature* **2020**, *579* (7798), 229–232.
(43) Cruz-Félix, A. S.; Santiago-Alvarado, A.; Márquez-García, J.; González-García, J. PDMS Samples Characterization with Variations of Synthesis Parameters for Tunable Optics Applications. *Heliyon* **2019**, *5* (12), No. e03064.
(44) Allen, J. L.; Borodin, O.; Seo, D. M.; Henderson, W. A. Combined Quantum Chemical/Raman Spectroscopic Analyses of Li+ Cation Solvation: Cyclic Carbonate Solvents—Ethylene Carbonate and Propylene Carbonate. *J. Power Sources* **2014**, *267*, 821–830.
(45) Han, S. D.; Yun, S. H.; Borodin, O.; Seo, D. M.; Sommer, R. D.; Young, V. G.; Henderson, W. A. Solvate Structures and Computational/Spectroscopic Characterization of LiPF6 Electrolytes. *J. Phys. Chem. C* **2015**, *119* (16), 8492–8500.
(46) Cresce, A. V.; Russell, S. M.; Borodin, O.; Allen, J. A.; Schroeder, M. A.; Dai, M.; Peng, J.; Gobet, M. P.; Greenbaum, S. G.; Rogers, R. E.; Xu, K. Solvation Behavior of Carbonate-Based Electrolytes in Sodium Ion Batteries. *Phys. Chem. Chem. Phys.* **2016**, *19* (1), 574–586.
(47) Ha, Y.; Tremolet De Villers, B. J.; Li, Z.; Xu, Y.; Stradins, P.; Zakutayev, A.; Burrell, A.; Han, S. D. Probing the Evolution of Surface Chemistry at the Silicon-Electrolyte Interphase via in Situ Surface-Enhanced Raman Spectroscopy. *J. Phys. Chem. Lett.* **2020**, *11* (1), 286–291.
(48) Su, L.; Zhao, X.; Yi, M.; Charalambous, H.; Celio, H.; Liu, Y.; Manthiram, A.; Su, L.; Zhao, X.; Yi, M.; Celio, H.; Liu, Y.; Manthiram, A.; Charalambous, H. Uncovering the Solvation Structure of LiPF6-Based Localized Saturated Electrolytes and Their Effect on LiNiO2-Based Lithium-Metal Batteries. *Adv. Energy Mater.* **2022**, *12* (36), No. 2201911.
(49) Song, H. Y.; Fukutsuka, T.; Miyazaki, K.; Abe, T. In Situ Raman Investigation of Electrolyte Solutions in the Vicinity of Graphite Negative Electrodes. *Phys. Chem. Chem. Phys.* **2016**, *18* (39), 27486–27492.
(50) Fortunato, B.; Mirone, P.; Fini, G. Infrared and Raman Spectra and Vibrational Assignment of Ethylene Carbonate. *Spectrochim. Acta A* **1971**, *27* (9), 1917–1927.
(51) Yaghobian, F.; Korn, T.; Schüller, C. Frequency Shift in Graphene-Enhanced Raman Signal of Molecules. *ChemPhysChem* **2012**, *13* (18), 4271–4275.
(52) Cortijo-Campos, S.; Ramírez-Jiménez, R.; Climent-Pascual, E.; Aguilar-Pujol, M.; Jiménez-Villacorta, F.; Martínez, L.; Jiménez-Riobóo, R.; Prieto, C.; de Andrés, A. Raman Amplification in the Ultra-Small Limit of Ag Nanoparticles on SiO2 and Graphene: Size and Inter-Particle Distance Effects. *Mater. Des.* **2020**, *192*, No. 108702.
(53) Yang, L.; Ren, Z.; Zhang, M.; Song, Y.; Li, P.; Qiu, Y.; Deng, P.; Li, Z. Three-Dimensional Porous SERS Powder for Sensitive Liquid and Gas Detections Fabricated by Engineering Dense "Hot Spots" on Silica Aerogel. *Nanoscale Adv.* **2021**, *3* (4), 1012–1018.

https://doi.org/10.1021/acsami.6c08906
ACS Appl. Mater. Interfaces 2026, 18, 43345–43356

(54) Liu, Y.; Hu, Y.; Zhang, J. Few-Layer Graphene-Encapsulated Metal Nanoparticles for Surface-Enhanced Raman Spectroscopy. *J. Phys. Chem. C* **2014**, *118* (17), 8993–8998.
(55) Xu, W.; Ling, X.; Xiao, J.; Dresselhaus, M. S.; Kong, J.; Xu, H.; Liu, Z.; Zhang, J. Surface Enhanced Raman Spectroscopy on a Flat Graphene Surface. *Proc. Natl. Acad. Sci. U. S. A.* **2012**, *109* (24), 9281–9286.
(56) Xu, S.; Wang, J.; Zou, Y.; Liu, H.; Wang, G.; Zhang, X.; Jiang, S.; Li, Z.; Cao, D.; Tang, R. High Performance SERS Active Substrates Fabricated by Directly Growing Graphene on Ag Nanoparticles. *RSC Adv.* **2015**, *5* (110), 90457–90465.
(57) Ling, X.; Moura, L. G.; Pimenta, M. A.; Zhang, J. Charge-Transfer Mechanism in Graphene-Enhanced Raman Scattering. *J. Phys. Chem. C* **2012**, *116* (47), 25112–25118.
(58) Huang, S.; Ling, X.; Liang, L.; Song, Y.; Fang, W.; Zhang, J.; Kong, J.; Meunier, V.; Dresselhaus, M. S. Molecular Selectivity of Graphene-Enhanced Raman Scattering. *Nano Lett.* **2015**, *15* (5), 2892–2901.
(59) Chakradhar, A.; Sivapragasam, N.; Nayakasinghe, M. T.; Burghaus, U. Adsorption Kinetics of Benzene on Graphene: An Ultrahigh Vacuum Study. *J. Vac. Sci. Technol., A* **2016**, *34* (2).
(60) Karton, A. π–π Interactions between Benzene and Graphene by Means of Large-Scale DFT-D4 Calculations. *Chem. Phys.* **2022**, *561*, No. 111606.
(61) Lechner, C.; Sax, A. F. Adhesive Forces Between Aromatic Molecules and Graphene. *J. Phys. Chem. C* **2014**, *118* (36), 20970–20981.
(62) Rattanabut, C.; Wongwiriyapan, W.; Muangrat, W.; Bunjongpru, W.; Phonyiem, M.; Song, Y. J. Graphene and Poly(Methyl Methacrylate) Composite Laminates on Flexible Substrates for Volatile Organic Compound Detection. *Jpn. J. Appl. Phys.* **2018**, *57* (4S), No. 04FP10.
(63) Spotte-Smith, E. W. C.; Petrocelli, T. B.; Patel, H. D.; Blau, S. M.; Persson, K. A. Elementary Decomposition Mechanisms of Lithium Hexafluorophosphate in Battery Electrolytes and Interphases. *ACS Energy Lett.* **2022**, *8* (1), 347–355.
(64) Pokorný, V.; Štejfa, V.; Fulem, M.; Červinka, C.; Růžička, K. Vapor Pressures and Thermophysical Properties of Ethylene Carbonate, Propylene Carbonate, γ-Valerolactone, and γ-Butyrolactone. *J. Chem. Eng. Data* **2017**, *62* (12), 4174–4186.
(65) Figaro USA, Inc. *TGS 2620 – for the Detection of Solvent Vapors (Product Information Sheet)*. https://www.figarosensor.com/product/entry/tgs2620.html (accessed 2026-06-17).
(66) Du, X.; Yang, B.; Lu, Y.; Guo, X.; Zu, G.; Huang, J. Detection of Electrolyte Leakage from Lithium-Ion Batteries Using a Miniaturized Sensor Based on Functionalized Double-Walled Carbon Nanotubes. *J. Mater. Chem. C Mater.* **2021**, *9* (21), 6760–6765.
(67) Lupan, O.; Magariu, N.; Santos-Carballal, D.; Ababii, N.; Offermann, J.; Pooker, P.; Hansen, S.; Siebert, L.; de Leeuw, N. H.; Adelung, R. Development of 2-in-1 Sensors for the Safety Assessment of Lithium-Ion Batteries via Early Detection of Vapors Produced by Electrolyte Solvents. *ACS Appl. Mater. Interfaces* **2023**, *15* (22), 27340–27356.
(68) Su, H.; Yang, H.; Ma, C.; Tang, J.; Zhu, C.; Wang, X.; Zeng, D. High Response and Selectivity of the SnO2 Nanobox Gas Sensor for Ethyl Methyl Carbonate Leakage Detection in a Lithium-Ion Battery. *ACS Sens.* **2024**, *9* (1), 444–454.
(69) Zhao, L.; Yu, C.; Wu, X.; Zuo, M.; Zhang, Q.; Dong, Q.; Ding, L. Computational Screening Guiding the Development of a Covalent-Organic Framework-Based Gas Sensor for Early Detection of Lithium-Ion Battery Electrolyte Leakage. *ACS Appl. Mater. Interfaces* **2025**, *17*, 10108–10117.
(70) Sheng, S.; Li, H.; Zhang, Y.; Li, L.; Xiao, K.; Huang, X.; Liu, Y.; Xu, W.; Li, Z.; Yan, L.; Yan, Z.; Huang, Y.; Sun, Q.; Sheng, S.; Li, H.; Zhang, Y.; Li, L.; Xiao, K.; Huang, X.; Liu, Y.; Xu, W.; Li, Z.; Yan, L.; Yan, Z.; Huang, Y.; Sun, Q. Early Detection of Lithium Battery Leakage Using a Highly Sensitive in Situ ZIF-8 Membrane-Coated Micro-Nano Optical Fibre. *Light Adv. Manuf.* **2025**, *6* (1), 130–141.

https://doi.org/10.1021/acsami.6c08906
ACS Appl. Mater. Interfaces 2026, 18, 43345–43356